

# Helical Bilayer Nanographenes: Impact of the Helicene Length on the Structural, Electrochemical, Photophysical, and Chiroptical Properties

Patricia Izquierdo-García, Jesús M. Fernández-García, Samara Medina Rivero, Michal Šámal, Jiří Rybáček, Lucie Bednárová, Sergio Ramírez-Barroso, Francisco J. Ramírez, Rafael Rodríguez, Josefina Perles, David García-Fresnadillo, Jeanne Crassous, Juan Casado, Irena G. Stará, and Nazario Martín\*



Cite This: <https://doi.org/10.1021/jacs.3c01088>



Read Online

ACCESS |



Metrics & More

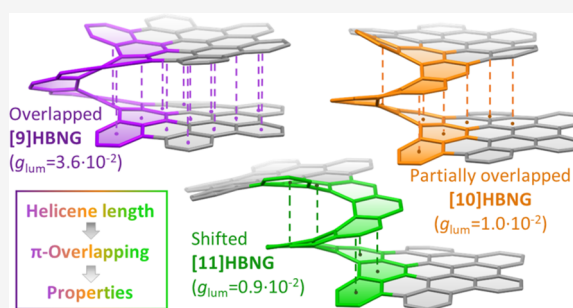


Article Recommendations



Supporting Information

**ABSTRACT:** Helical bilayer nanographenes (HBNGs) are chiral  $\pi$ -extended aromatic compounds consisting of two  $\pi$ -stacked hexabenzocoronenes (HBCs) joined by a helicene, thus resembling van der Waals layered 2D materials. Herein, we compare [9]HBNG, [10]HBNG, and [11]HBNG helical bilayers endowed with [9], [10], and [11]helicenes embedded in their structure, respectively. Interestingly, the helicene length defines the overlapping degree between the two HBCs (number of benzene rings involved in  $\pi$ - $\pi$  interactions between the two layers), being 26, 14, and 10 benzene rings, respectively, according to the X-ray analysis. Unexpectedly, the electrochemical study shows that the lesser  $\pi$ -extended system [9]HBNG shows the strongest electron donor character, in part by interlayer exchange resonance, and more red-shifted values of emission. Furthermore, [9]HBNG also shows exceptional chiroptical properties with the biggest values of  $g_{\text{abs}}$  and  $g_{\text{lum}}$  ( $3.6 \times 10^{-2}$ ) when compared to [10]HBNG and [11]HBNG owing to the fine alignment in the configuration of [9]HBNG between its electric and magnetic dipole transition moments. Furthermore, spectroelectrochemical studies as well as the fluorescence spectroscopy support the aforementioned experimental findings, thus confirming the strong impact of the helicene length on the properties of this new family of bilayer nanographenes.



## INTRODUCTION

The discovery of graphene by Geim and Novoselov in 2004 laid the foundations of the science of single-atom-thick layer materials or 2D materials.<sup>1</sup> Since this historic milestone, the development of atomically thin layer materials—with carbon and other elements of the periodic table—has been successfully achieved along the last recent years. The new family of monoelemental 2D materials, namely, graphyne,<sup>2</sup> borophene,<sup>3</sup> germanene,<sup>4</sup> silicene,<sup>5</sup> stanene,<sup>6</sup> plumbene,<sup>7</sup> phosphorene,<sup>8</sup> antimonene,<sup>9</sup> and bismuthene,<sup>10</sup> was rapidly followed by the search for multielemental layered materials.<sup>11</sup> The main expectation is that, given their exceptional properties, 2D materials could replace conventional semiconductors to deliver a new generation of electronics with applications in sensors,<sup>12</sup> low-cost organic solar cells,<sup>13</sup> LEDs,<sup>14</sup> transistors,<sup>15</sup> piezoelectrics,<sup>16</sup> superconductors,<sup>17</sup> or magnetism,<sup>18</sup> among others.

Chemically, the pristine forms of these materials show strong in-plane covalent bonds and weak out-of-plane van der Waals (vdW) interactions. The stacking of several layers generates pseudocrystalline materials known as vdW layered solids.<sup>19</sup>

Remarkably, the twist angle between the layers of stacked 2D materials produces a moiré pattern, forming a superlattice with a new band structure that dramatically affects the electronic properties of the material.<sup>20</sup> In this regard, Jarillo-Herrero et al. have recently reported that a two-layered graphene having a “magic angle” of  $1.1^\circ$  between the two honeycomb lattices shows superconductivity at 1.7 K.<sup>21</sup> This finding represents an important landmark in the search for high-temperature superconductivity.<sup>22</sup>

Interestingly, the band gap properties of 2D materials can also be modified by the quantum confinement of the electrons in dimensionally reduced structures (1D, nanoribbons; 0D, quantum dots).<sup>23</sup> As a consequence of the edge effects in nanosized fragments of graphene, the so-called nanographenes

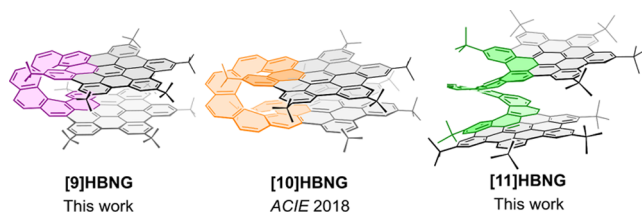
Received: January 30, 2023

(NGs), it is possible to open up the zero band gap of graphene, leading to semiconductor materials with potential applications in organic electronics.<sup>24</sup>

Additionally, the bottom-up synthesis of monodisperse molecular NGs by using the arsenal of organic chemistry reactions allows controlling at will the size, morphology, and the *ad hoc* incorporation of defects in the final structure of the molecule. This synthetic control allows, in turn, the fine-tuning of chemical, optical, and electronic properties.<sup>25</sup> In the last recent years, a broad variety of molecular NGs have been synthesized by this methodology, covering a wide range of shapes, from the straightforward planar NGs<sup>26</sup> to curved,<sup>27</sup> twisted,<sup>28</sup> or helically arranged molecular NGs.<sup>29</sup> The incorporation of curvature, strain, or helicity in NGs may introduce asymmetry in the structures, leading to the appearance of stereoisomeric forms,<sup>30</sup> that open the possibility of new applications derived from their chiroptical properties.<sup>31</sup>

The combination of both, stacked vdW materials and quantum confinement of electrons in NGs, leads to a new type of molecular bilayer NGs whose properties remain basically unexplored and scarcely reported.<sup>32</sup> In this regard, some of the co-authors pioneered the topic,<sup>33</sup> and our research group has recently reported a helical bilayer nanographene (HBNG) [10]HBNG inspired by the  $\pi$ -extended connection of a [6]helicene moiety and two hexabenzocoronene (HBC) units (Chart 1).<sup>34</sup> The length of the resulting [10]helicene places the HBC fragments in a AA stacking (AB for graphite) disposition.

**Chart 1. HBNGs Endowed with Helicenes of Different Length, which Results in Different Degrees of  $\pi$ -Overlapping between the HBC Layers**



Herein, we report on the synthesis of new molecular bilayer NGs starting from [5]helicene and [7]helicene.<sup>35</sup> Both systems lead to the expected formation of the respective helical bilayers [9]HBNG and [11]HBNG (Chart 1). The different lengths of the helicene moiety ([9] and [11]helicenes, respectively) make the HBC layers to be disposed with a significantly different degree of overlapping between them. This allows us to address electronic features arising from the co-facial coupling such as mixed valence effects in the oxidized state, excimer-like formation in the excited state, and Raman vibrational properties comparable to graphene and multilayer graphene. Since the final bilayer NGs are obtained as racemates, a careful separation of their respective enantiomers has been performed by using chiral HPLC. Interestingly, the structural differences have a strong impact on their chiroptical, photophysical, electrochemical, and spectroelectrochemical properties, which are discussed in the light of the previously synthesized [10]helicene-containing bilayer [10]HBNG, whose new properties are also reported for the first time in this work. Singularly, [9]HBNG displays one of the largest chiral photoluminescence dissymmetry factors ( $g_{lum}$ ) reported for pure hydrocarbons. This experimental finding arises from an

alignment of the electric and magnetic transition vectors, stemming from the fine balance between vertical and layered  $\pi$ -conjugations.

## RESULTS AND DISCUSSION

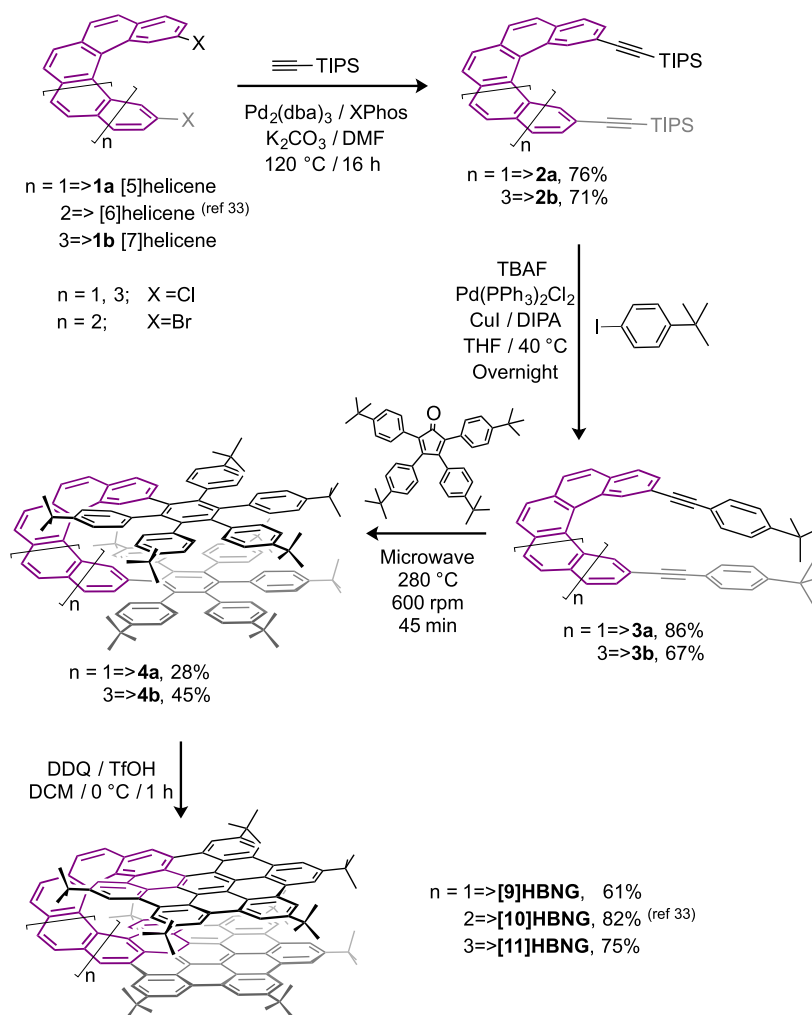
Inspired by the intriguing modification of the properties of 2D materials by twisting stacking bilayers, we decided to unveil the structural, chiroptical, photophysical, electrochemical, and spectroelectrochemical properties of this family of HBNGs. For this purpose, we designed a bottom-up synthetic strategy, in which starting from dihalo[n]helicenes with different lengths (dichloro[5]helicene **1a**<sup>36</sup> and dichloro[7]helicene **1b**<sup>37</sup>),<sup>38</sup> it is possible to control the length of the resulting helicene in the final HBNG ([9]HBNG and [11]HBNG) and, therefore, the  $\pi$ -overlapping between the planar HBC layers (Scheme 1).

**Synthetic Procedure.** The preparation of [9]HBNG and [11]HBNG was achieved using our previously reported synthetic strategy employed to prepare [10]HBNG (Scheme 1). These rapid syntheses consist of only four reaction steps starting from dichloro[5]helicene **1a** and dichloro[7]helicene **1b**. Pd-catalyzed Sonogashira cross-coupling reaction with (triisopropylsilyl)acetylene led to the protected dialkynylhelicenes **2a** and **2b**, respectively. Thereafter, a new Sonogashira reaction with 4-*tert*-butyliodobenzene, with in situ deprotection of the TIPS groups using TBAF, added a benzene ring to each triple bond affording **3a** and **3b**. Then, Diels–Alder cycloaddition of tetrakis-(4-*tert*-butylphenyl)cyclopentadienone to the alkynes, followed by the retrocheletropic liberation of carbon monoxide, led to the corresponding helicenes endowed with two pentaphenylbenzene groups **4a** and **4b**, respectively. Finally, Scholl cyclodehydrogenation using 2,3-dichloro-5,6-dicyano-1,4-benzoquinone and trifluoromethanesulfonic acid formed 12 new C–C bonds, shaping the two HBC layers and extending the helicene backbone from [5]- and [7]- to [9]- and [11]helicene, respectively, yielding the desired [9]HBNG and [11]HBNG compounds with good yields (61 and 75%, respectively). The final new molecules have been characterized by <sup>1</sup>H and <sup>13</sup>C NMR, Fourier-transform infrared, and high-resolution mass spectrometry. The loss of 24 units in the molecular weight of **4a** (MW = 1751) and **4b** (MW = 1851) when they afford the final products [9]HBNG (MW = 1727) and [11]HBNG (MW = 1827) clearly indicates the formation of 12 C–C bonds in the Scholl reaction step and reveals the total graphitization of the HBC moieties. Additionally, <sup>1</sup>H and <sup>13</sup>C NMR spectra only show the signals corresponding to a half of the molecule in both cases, revealing the presence of a C<sub>2</sub> rotational axis (Figures S7 and S8, see the Supporting Information).

The structures of [9]HBNG and [11]HBNG were solved by single-crystal X-ray diffraction (Figure 1). In both cases, centrosymmetric crystals containing *M* and *P* isomers were obtained from their respective racemic mixtures, unlike what happened in [10]HBNG, where the two isomers were spontaneously separated by crystallization, yielding enantiopure acentric crystals.<sup>34</sup>

The comparison of the three crystal structures reveals some interesting facts and explains the differences observed in their physical properties (see the sections below). As expected, the length of the helicene linker was found to be crucial in achieving a convenient location of the two HBC layers of the molecules and proved to influence the overlap of the two NG fragments.

**Scheme 1. Synthesis of HBNGs [9]HBNG and [11]HBNG from Dichloro[5]helicene 1a and Dichloro[7]helicene 1b, Respectively**



Thus, a total of 26 benzene rings in [9]HBNG are involved in extended  $\pi$ - $\pi$  interactions, resulting in an effectively through-space overlapped bilayer (i.e., see this effect in the zenithal view in Figure 1, middle left, and Figure S9, left). Consequently, the molecule adopts a remarkable U-shape from a side view (Figure 1, top), with a small interplanar angle of  $2.37^\circ$  between the layers of the HBC subunits and a distance between the pivotal atoms of opposite <sup>t</sup>Bu groups of 5.185 Å (C45–C127). Due to geometrical constraints, the rings of the two layers are staggered, with an average distance of 3.63 Å between the centroids of one layer and the opposite plane (Figures S9 and S10 and Table S5, see the Supporting Information).

In [10]HBNG, the length of the helicene allows a partially overlapped AA-stacking of the two NG layers, with 14 rings participating in  $\pi$ - $\pi$  interactions seen from a top view (Figure 1, middle, and Figure S9, middle). The similarity with an AA-type graphene stacking allowed the determination of an average distance of 3.54 Å between the matching centroids of opposite layers (Table S5, see the Supporting Information). The angle between the HBC planes has a value of  $5.19^\circ$ , giving a V-shape to [10]HBNG (Figure 1, top, and Figure S9, see the Supporting Information), while the distance between the opposing <sup>t</sup>Bu groups is 12.436 Å (C99–C127) due to the

skewed structure arising from the partial overlap between HBC subunits.

In the case of [11]HBNG, the extension of the helicene linker forces the two HBC layers to separate, resulting in a shifted bilayer that presents  $\pi$ - $\pi$  interactions between 10 benzene rings (Figure S9, right). In this HBNG, only one of the peripheral rings from each layer can participate in these bonds, and the mean distance between centroids involved in  $\pi$ - $\pi$  interactions is 3.41 Å. The length of the molecule is the largest of the three (C45–C131 = 23.368 Å), and it also displays the highest angle between the two HBC layers ( $11.51^\circ$ ), generating a structure with a distorted Z-shaped lateral view.

A consequence of the diverse shapes displayed by the three HBNGs is the different packing observed for these molecular NGs in their crystal structures (Figure 1, bottom). [9]HBNG molecules are closely located in pairs of *M* and *P* isomers (Figure S11, see the Supporting Information) due to the strong intermolecular  $\pi$ - $\pi$  interactions (3.359 Å). Weak C–H $\cdots\pi$  interactions join the pairs of molecules, leaving huge voids, where disordered solvent molecules are lodged. Besides, columns of molecules are located at a perpendicular angle in the crystal structure of [10]HBNG, owing to C–H $\cdots\pi$  interactions. Finally, the packing of [11]HBNG is achieved by C–H $\cdots\pi$  supramolecular interactions not only between the

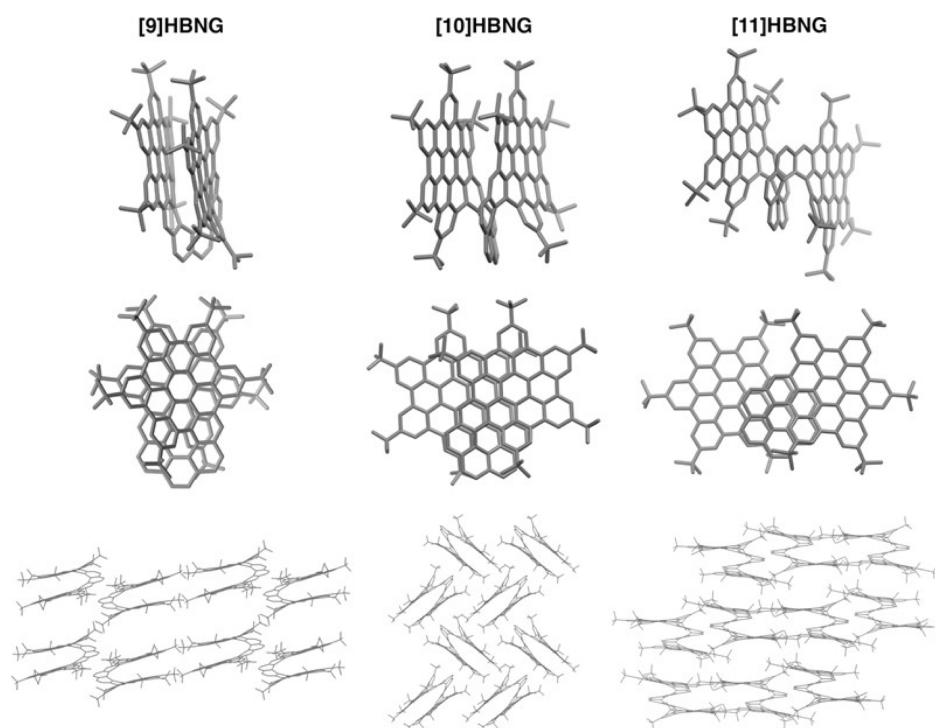


**Figure 1.** Molecular structures of compounds [9]HBNG, [10]HBNG,<sup>34</sup> and [11]HBNG obtained by X-ray diffraction from single crystals (hydrogen atoms have been omitted for clarity). Lateral view (top), zenithal view (middle), and packing of the columns of molecules of [9]HBNG (along the [010] direction), [10]HBNG (along the [001]), and [11]HBNG (along [011]) (bottom).

HBNGs themselves but also between HBNGs and the interstitial dichloroethane molecules, yielding alternating homochiral columns in the [010] direction of *M* and *P* enantiomers (Figure S12).

**Electrochemical and Spectroelectrochemical Properties.** The electrochemical properties of [9]HBNG, [10]HBNG, and [11]HBNG were evaluated by cyclic voltammetry (CV, Figure 2) in a 0.1 M solution of

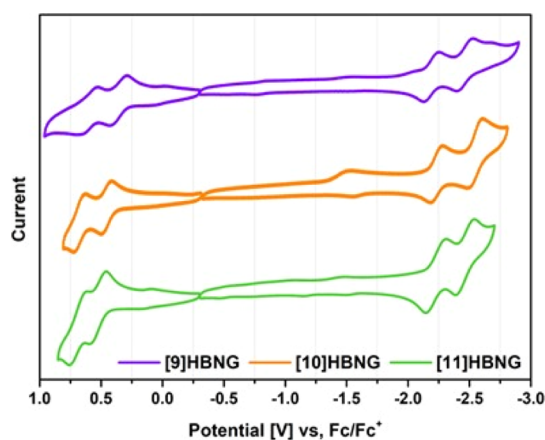


**Figure 2.** Cyclic voltammograms of HBNGs [9]HBNG, [10]HBNG, and [11]HBNG vs Fc/Fc<sup>+</sup> in toluene/CH<sub>3</sub>CN (4:1).

tetrabutylammonium hexafluorophosphate (i.e., Bu<sub>4</sub>NPF<sub>6</sub>) as supporting electrolyte, in a toluene/acetonitrile 4:1 mixture at room temperature. Table 1 shows the respective reduction and oxidation potentials vs Fc/Fc<sup>+</sup> compared to hexa-*tert*-butylhexa-*peri*-hexabenzocoronene <sup>t</sup>Bu-HBC as the reference.

**Table 1. First Oxidation and Reduction Potential Values of <sup>t</sup>Bu-HBC and Molecular NGs [9]HBNG, [10]HBNG, and [11]HBNG vs Fc/Fc<sup>+</sup> at Room Temperature**

	$E_{\text{ox}}^1$ (V)	$E_{\text{ox}}^2$ (V)	$E_{\text{red}}^1$ (V)	$E_{\text{red}}^2$ (V)
<sup>t</sup> Bu-HBC	0.75		-2.24	-2.40
[9]HBNG	0.35	0.59	-2.18	-2.46
[10]HBNG	0.46	0.67	-2.23	-2.55
[11]HBNG	0.52	0.69	-2.22	-2.46

In all three cases, two quasi-reversible oxidation waves and two quasi-reversible reduction waves are observed. The first oxidation potential follows the order [9]HBNG (0.35 V) < [10]HBNG (0.46 V) < [11]HBNG (0.52 V). Interestingly, the observed trend is the reverse of that expected according to the extension of the  $\pi$ -conjugation of the helicene moiety. Compared to <sup>t</sup>Bu-HBC (0.75 V), these bilayer NGs are significantly better electron donors. The oxidation potential variation seems to indicate that the larger the  $\pi$ - $\pi$  overlapping of the two layers, the lower the oxidation potential values. This experimental finding could be accounted for by the fact that the radical cation and the dication species ( $E_{\text{ox}}^1$  and  $E_{\text{ox}}^2$ , respectively) are stabilized through the interaction between the two graphitized layers. This observation agrees with the location of the HOMO on the bilayer moieties.<sup>34</sup> Regarding the reduction potentials, previous studies on the [10]HBNG bilayer show that the reduction occurs, mainly, on the helicene region where the LUMO is located,<sup>29d</sup> and reduction waves at -2.18, -2.23, and -2.22 V are observed for [9]HBNG, [10]HBNG, and [11]HBNG, respectively.

Density functional theory calculations of the HOMO and LUMO topologies and energies have been carried out and are shown in Figure S26. A nice correlation is observed in the values of the HOMO and LUMO energies with the variation

of the experimental oxidation and reduction potentials. In particular, the LUMOs of the three compounds are mainly located in the helicene moiety. In this regard, it is the scarce through bond conjugation along the helicene on the three compounds that justifies the small changes observed in their reduction potentials. On the other hand, the HOMOs are mainly located in the HBC units, and their energies vary in line with the measured oxidation potentials. Nonetheless, in order to account for the quantitative changes, through-space  $\pi$ -delocalization between the two layers in the radical cation needs to be considered.

UV–vis–NIR spectroelectrochemical measurements of the three compounds have been carried out in a thin-layer spectroelectrochemical cell (Figures 3 and S17, see the

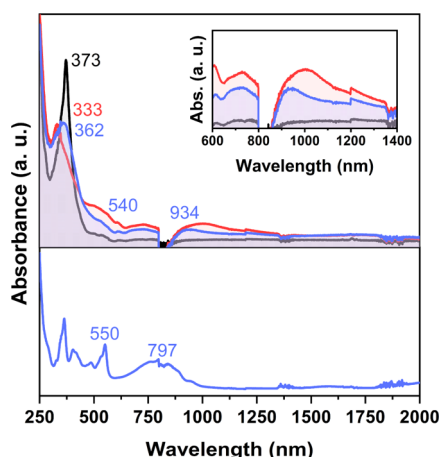


**Figure 3.** UV–vis–NIR electronic absorption spectra obtained upon electrochemical oxidation of [9]HBNG in a 0.1 M  $\text{Bu}_4\text{NPF}_6$  solution in  $\text{CH}_2\text{Cl}_2$  at room temperature by using a thin-layer spectroelectrochemical cell. Black shadowed lines correspond to neutral species; blue/red shadowed lines correspond to the first/second oxidized species. UV–vis–NIR electronic absorption spectrum of the  ${}^t\text{Bu-HBC}$  radical cation is also shown (bottom, blue line) for reference.

**Supporting Information**). The first oxidation of [9]HBNG leads to the appearance of two distinctive absorption bands at 934 and 540 nm that compare with those of the radical cation of  ${}^t\text{Bu-HBC}$  at 797 and 550 nm (Figure 3, bottom, and Figure S17a, see the **Supporting Information**). The observed 797  $\rightarrow$  934 nm red shift agrees with the smaller oxidation potential of [9]HBNG relative to  ${}^t\text{Bu-HBC}$ . The significant decrease of the oxidation potential observed for [9]HBNG might reveal a twofold effect: (i) the involvement of the helicene moiety in the oxidation and (ii) based on the previous wavelength red shift of the absorption bands, an inter-layer charge delocalization, which eventually contributes to lower the oxidation potential.

In the case of the second oxidation process, which is only observed in [9]HBNG (i.e., not in  ${}^t\text{Bu-HBC}$ ), this further oxidation provokes a blue shift of the main UV–vis–NIR absorption bands, in line with the confinement of one radical cation in each HBC moiety due to charge repulsion in the dication state. The strongest absorption band of the neutral at 373 nm in [9]HBNG progressively blue-shifts on oxidation to 362 and 333 nm in the first and second oxidized species, respectively (Figure 3). Given that the strong band in the neutral state is composed of transitions emerging from the helicene and the HBC moieties, the notable variation of this

band with oxidation supports that, upon electron extraction, the charge is jointly stabilized by the two moieties.

The electronic absorption spectra of [11]HBNG in the two oxidation states display a progressive red shift with increasing oxidation for the vis–NIR bands, in accordance with the charge being stabilized in a similar way in the two redox species of [11]HBNG.

#### Photophysical Properties of the Racemic Mixture.

The absorption spectra of the HBNGs [9]HBNG (overlapped bilayer), [10]HBNG (partially overlapped), and [11]HBNG (shifted bilayer) and of the monolayer NG,  ${}^t\text{Bu-HBC}$ , are shown in Figure 4. Their

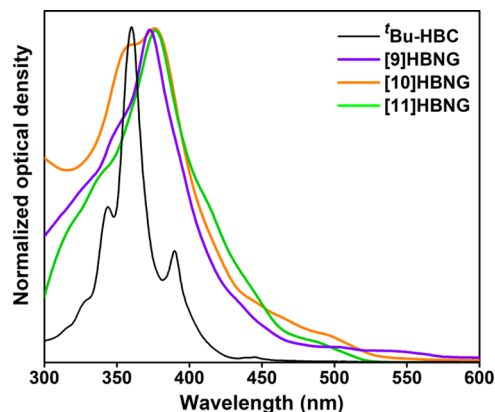


**Figure 4.** Absorption spectra of  ${}^t\text{Bu-HBC}$  and of HBNGs [9]HBNG, [10]HBNG, and [11]HBNG in  $\text{CHCl}_3$ .

corresponding peak/shoulder wavelengths and absorption coefficients are shown in Table 2. Shoulders were determined from the second derivative of the absorption spectrum. The rigid and flat  ${}^t\text{Bu-HBC}$  monolayer NG shows a structured absorption spectrum with a vibronic fine structure and a maximum at 360 nm, while the HBNGs [9]HBNG, [10]HBNG, and [11]HBNG display non-structured and broader absorption spectra, extended to 569, 557, and 518 nm, respectively (absorption tails with at least 1% absorption with respect to that of the maximum), with slightly bathochromically shifted maxima in the 373–377 nm interval. Interestingly, the HBNGs show allowed electronic transitions in the visible region above 400 nm, with absorption coefficients  $>10^4 \text{ M}^{-1} \text{ cm}^{-1}$ . Conversely, the planar  ${}^t\text{Bu-HBC}$  monolayer NG exhibits forbidden transitions in the visible region ( $\epsilon \sim 10^3 \text{ M}^{-1} \text{ cm}^{-1}$ ). Therefore, the more intense and red-shifted absorption bands observed in the visible region reflect the direct involvement of both helicene and HBC moieties in the optical properties of HBNGs, in good agreement with the previous literature on curved molecular NGs containing both subunits.<sup>27c</sup>

Regarding the fluorescence of the HBNGs, their corresponding emission spectra are shown in Figure 5. Compared to  ${}^t\text{Bu-HBC}$ , they show broader, non-structured, and red-shifted emission bands, with full width at half-maximum (fwhm) values in the  $\sim 2500\text{--}3000 \text{ cm}^{-1}$  interval (cf.  $\sim 1600 \text{ cm}^{-1}$  for  ${}^t\text{Bu-HBC}$ ). The emission spectra have two main features: (i) in shape, they resemble more the emission spectra of helicenes with one molecular band disclosing vibronic resolution and (ii) the pronounced broadening is more typical of excimer-type emissions. According to (ii), the most red-shifted excimer-like band is for [9]HBNG, in line with the greater propensity to

**Table 2. Data from Absorption Spectra of the HBNGs [9]HBNG, [10]HBNG, and [11]HBNG and of the Monolayer NG <sup>t</sup>Bu-HBC in Chloroform**

	$\lambda_{\text{abs}}/\text{nm}$ ( $\epsilon/\text{M}^{-1}\text{cm}^{-1}$ ) <sup>a</sup>
[9]HBNG	349 (94,600); 373 (136,000); 392 (86,300); 435 (20,600); 502 (6200); and 542 (4700)
[10]HBNG	360 (98,600); 377 (103,900); 415 (38,800); 446 (18,700); 462 (14,400); and 494 (8700)
[11]HBNG	339 (70,800); 377 (125,000); 415 (58,200); 444 (26,100); and 491 (7300)
<sup>t</sup> Bu-HBC	344 (63,750); 360 (141,700); 390 (46,350); 439 (1600); 441 (1650); and 445 (1800)

<sup>a</sup> $\lambda_{\text{abs}}/\text{nm}$  ( $\pm 1$  nm) ( $\epsilon/\text{M}^{-1}\text{cm}^{-1}$ ) ( $\pm 10\%$ ).

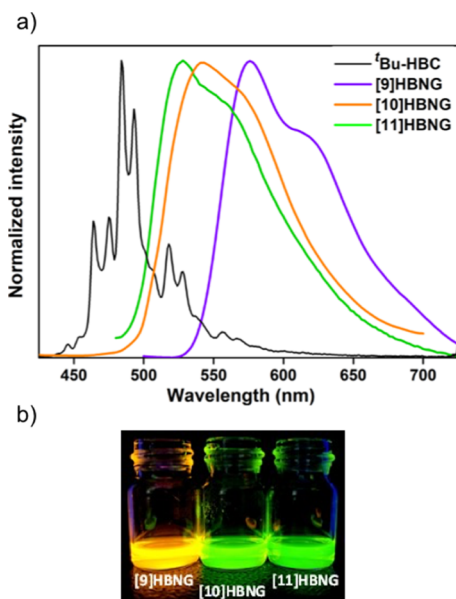


**Figure 5.** (a) Fluorescence spectra of <sup>t</sup>Bu-HBC and of HBNGs [9]HBNG, [10]HBNG, and [11]HBNG in CHCl<sub>3</sub>. (b) Samples of [9]HBNG, [10]HBNG, and [11]HBNG in CHCl<sub>3</sub> under 365 nm lamp irradiation (bottom).

form interlayer interactions. According to (i), the three emissions have clear helicene contributions. Remarkably, [9]HBNG (overlapped bilayer), the bilayer helicene with the lowest number of fused benzene rings (9) and most overlapped  $\pi$ -structure (i.e., larger  $\pi$ - $\pi$  interactions), displays the most bathochromically shifted fluorescence (pointing to a more stable singlet excited state as compared to [10]HBNG and [11]HBNG). It is likely that structural differences among the bilayer NGs considering the increasing number of benzene rings within the helicene framework, at the level of their torsional angle or their interplanar angle, resulting in different interlayer interactions, might influence the distinct fluorescence shifts and, therefore, the general photophysics of the HBNGs. Emission data of the monolayer NG <sup>t</sup>Bu-HBC and of the HBNGs [9]HBNG, [10]HBNG, and [11]HBNG are shown in Table 3. The Stokes' shifts of the bilayer NGs are 9419 cm<sup>-1</sup> (204 nm) for [9]HBNG, 8109 cm<sup>-1</sup> (187 nm) for [10]HBNG, and 7585 cm<sup>-1</sup> (154 nm) for [11]HBNG, while

the planar and more rigid monolayer NG <sup>t</sup>Bu-HBC shows the lowest Stokes' shift (7117 cm<sup>-1</sup>, 124 nm). This result agrees with the lower molecular stiffness of the bilayer NGs studied and, notably, points to the higher singlet excited state reorganization energy of [9]HBNG compared to [10]HBNG and, in particular, [11]HBNG (the one with the lowest degree of overlap).

The estimated optical energy gaps were obtained from the intersections between the normalized excitation and emission spectra of the HBNGs [9]HBNG, [10]HBNG, and [11]HBNG, as shown in Table 3. The values found are between 2.3 and 2.6 eV. The fluorescence quantum yields ( $\Phi_{\text{em}}$ ) of [9]HBNG, [10]HBNG, and [11]HBNG (0.22, 0.10, and 0.11, respectively) were determined at room temperature using N<sub>2</sub>-purged solutions with optical densities <0.1 at 395 nm, by comparison with the emission spectra of riboflavin in ethanol ( $\Phi_{\text{em}} = 0.30 \pm 0.03$ ).  $\Phi_{\text{em}}$  variation of the three HBNGs does not follow the energy gap law; however, they can be accounted for, in part, by the increasing contribution of the excimer-like emission which enlarges the fluorescence quantum yield in [9]HBNG despite having the smallest optical gap.

Regarding the time-resolved emission of HBNGs [9]HBNG, [10]HBNG, and [11]HBNG, fluorescence decay profiles in chloroform at room temperature are shown in Figure S18, see the Supporting Information. While [9]HBNG and [10]HBNG, the HBNGs with strongly and partially overlapped bilayers, required multiexponential fittings of the decay function, [11]HBNG, the one with a shifted bilayer, exhibited a monoexponential behavior. The discrete lifetime components ( $\tau_i$ ), pre-exponential factors ( $B_i$ ), zero-time intensities ( $I_i$ ), and averaged lifetimes (intensity-weighted,  $\tau_{\text{Int}}$  or amplitude-weighted,  $\tau_{\text{Amp}}$ ) are shown in Table S6, see the Supporting Information. The intensity-weighted average lifetimes of [9]HBNG (13.4 ns) and [10]HBNG (12.2 ns) determined at the wavelength of the emission intensity maximum display longer lifetimes than [11]HBNG (8.7 ns), which exhibits the most blue-shifted emission among the HBNGs, according to the less stable nature of its singlet excited state of higher energy.

From the amplitude-weighted fluorescence average lifetimes and fluorescence quantum yields, the radiative ( $k_r$ ) and non-radiative ( $k_{\text{nr}}$ ) deactivation rate constants of the respective singlet excited states were calculated (Table S7, see the

**Table 3. Data from the Excitation and Fluorescence Spectra of the HBNGs [9]HBNG, [10]HBNG, and [11]HBNG and of the Monolayer NG <sup>t</sup>Bu-HBC in Chloroform**

	$\lambda_{\text{em}}^{\text{max}}/\text{nm}$ (shoulder)	fwhm/cm <sup>-1</sup> (eV)	Stokes' shift/cm <sup>-1</sup> (eV)	$E_{0-0}/\text{eV}$	$\Phi_{\text{em}}$
[9]HBNG	575 (611)	2547 (0.32)	9419 (1.17)	2.35 $\pm$ 0.09	0.22 $\pm$ 0.02
[10]HBNG	543 (567)	2943 (0.36)	8109 (1.00)	2.49 $\pm$ 0.09	0.10 $\pm$ 0.01
[11]HBNG	528 (551)	3012 (0.37)	7585 (0.94)	2.58 $\pm$ 0.09	0.11 $\pm$ 0.01
<sup>t</sup> Bu-HBC	445, 454, 464, 475, 484, 493, 518, 528, (537), 556, and 567	1613 (0.20) <sup>27c</sup>	7117 (0.88)	2.65 $\pm$ 0.13 <sup>27c,39</sup>	0.02 $\pm$ 0.01

Supporting Information).<sup>40</sup> Interestingly, while all the  $k_r$  values are rather similar among the studied HBNGs (ca  $1-2 \times 10^7$  s<sup>-1</sup>), [10]HBNG and [11]HBNG, the molecular NGs with less bilayer overlaps, show the largest  $k_{nr}$  values ( $1-1.5 \times 10^8$  s<sup>-1</sup>), which could be due to their higher structural mobility because of their less overlapped nature compared to their more  $\pi$ -stacked and constrained counterpart [9]HBNG. As a result, it could be concluded that the greater the structural overlap between NG layers, the more the relative radiative deactivation is favored, leading to higher emission quantum yields and longer fluorescence lifetimes.

The Raman spectra of the three bilayer compounds (Figure 6) have been measured and obtained in the solid state by using

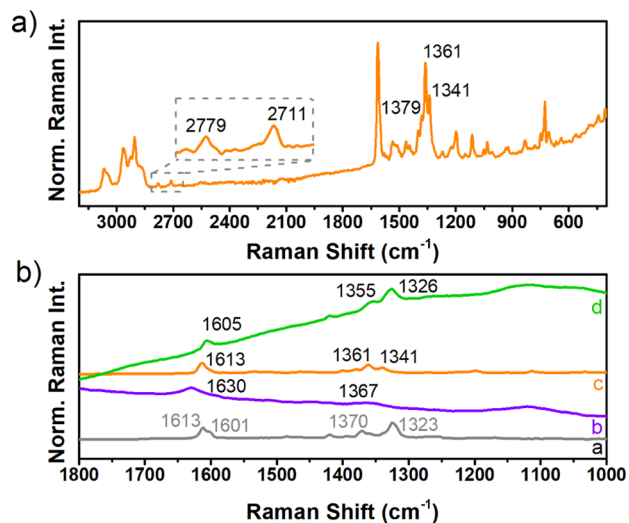


**Figure 6.** (a) Solid-state Raman spectrum at room temperature of [10]HBNG ( $\lambda_{exc} = 1064$  nm). (b) Raman spectra of (a) *t*Bu-HBC ( $\lambda_{exc} = 1064$  nm), (b) [9]HBNG ( $\lambda_{exc} = 325$  nm), (c) [10]HBNG ( $\lambda_{exc} = 1064$  nm), and (d) [11]HBNG in the solid state at room temperature.

different excitation laser wavelengths to avoid the adverse effect of fluorescence. Indeed, for [10]HBNG and [11]HBNG, the 1064 nm Raman spectra were obtained, whereas for [9]HBNG, large fluorescence and reabsorption in the NIR region precludes to obtain Raman spectra of quality. In contrast, however, these were obtained in [9]HBNG by excitation in the UV region with the 325 nm laser Raman line. The Raman spectra are all characterized by the presence of two main groups of bands at 1600 and 1350–1300 cm<sup>-1</sup> which are the typical G and D Raman bands which feature the vibrational Raman spectra of graphene and graphitic-like systems (see Figure S19 and Figure S20 in the Supporting Information for the theoretical Raman spectra and assignments of the most representative Raman bands in terms of vibrational normal modes). In particular, the 1064 nm Raman spectrum of [10]HBNG represents the molecular version of the complete Raman spectrum of graphene and multilayer graphene. The packing of graphene layers, one on top of the other, leads to the activation and appearance in the Raman spectra of new bands associated with the double and triple wavenumbers of the fundamental phonon Raman vibrations. The occurrence of such multiphonon (i.e., 2D and 2G) bands is an intrinsic characteristic observed on passing from graphene to multilayer graphene. In the Raman spectrum of [10]HBNG, the presence of overtones and combination bands is clearly observed, which

are the molecular equivalents of the multiphonon Raman bands in multilayered graphene.

Among the Raman spectra of the three bilayer compounds, that of [10]HBNG shows the largest similarity with that of *t*Bu-HBC in the wavenumber region of the G Raman band at 1613 cm<sup>-1</sup>, whereas the G band of [9]HBNG at 1630 cm<sup>-1</sup> is that with the largest difference relative to *t*Bu-HBC. The variation 1613 (*t*Bu-HBC)  $\rightarrow$  1630 ([9]HBNG) cm<sup>-1</sup> can result by the vibrational mixing of the C–C bond stretching of the HBC moiety with that of the helicene (Figure S20), an effect that might account for the wavenumber upshift of these Raman bands.

#### Chiroptical Properties of Enantioenriched HBNGs.

Racemic HBNGs [9]HBNG, [10]HBNG, and [11]HBNG were resolved by means of semipreparative CSP HPLC using the Chiralpak IE column and a mixture of heptane and 1% isopropyl alcohol in toluene. The purity and optical rotation of the separated enantiomers of [9]HBNG, [10]HBNG, and [11]HBNG are shown in Table 4. All enantioenriched samples

**Table 4.** Data from the Separation of the Racemic HBNGs by HPLC

	OR <sup>a</sup> [ $\alpha$ ] <sub>D</sub> <sup>20</sup>	10 <sup>2</sup> $\times$ $g_{abs}$	HPLC ee (%)
(+)-[9]HBNG	+6706	+3.6	98
(-)-[9]HBNG	-7120	-2.8	99
(+)-[10]HBNG	+2447	+1.4 <sup>b</sup>	73
(-)-[10]HBNG	-4480	-1.6	99
(+)-[11]HBNG	+4033	+1.0	99
(-)-[11]HBNG	-4270	-1.0	99

<sup>a</sup>Optical rotation in THF. In addition to the loss of the material during chromatography, especially in the case of [10]HBNG, there were residual solvents present in the resolved samples, mainly toluene and/or dichloromethane (Section 9, see the Supporting Information). The larger discrepancy in the absolute values of the optical rotations of the opposite enantiomers is due to the presence of residual solvents after HPLC separation, see the Supporting Information for details. <sup>b</sup>Corrected to optical purity (i.e., scaled by a factor of  $\sim 1.4$ ).

show excellent enantiomeric excess (ee) except for the case of (+)-[10]HBNG that shows 73% ee. Additionally, the chiroptical circular dichroism for the six enantioenriched samples was measured in THF ( $2.5 \times 10^{-5}$  M).

The CD spectra of [10]HBNG and [11]HBNG show mainly two critical points in the visible region at 380 and 450 nm, arising from the helicene linker and the HBC layers, respectively (Figure 7). However, CD spectra of [9]HBNG show three maxima or minima in the same region at 380, 400, and 530 nm; in this case, the contributions of the helicene linker and the HBC are mixed, indicating that the total overlap of the HBC layers can play an important role in the chiroptical properties (see below). Comparing the CD spectra of [10]HBNG with the previously described spectrum of *M*-[10]HBNG,<sup>34</sup> the absolute configuration of both enantiomers of [10]HBNG can be assigned as (*P*) for the dextrorotatory enantiomer and (*M*) for the levorotatory enantiomer.

Note that the absorption dissymmetry factors ( $g_{abs}$ ) are quite high ( $1-3.6 \times 10^{-2}$ ) and of the same order as the  $g_{lum}$  values (see below), reflecting small structural and electronic reorganization of the excited state prior to the emission process. In addition to the optical rotation and circular dichroism of chiral molecules, a particular focus has recently been put on their circularly polarized emission (CPL).<sup>41</sup>

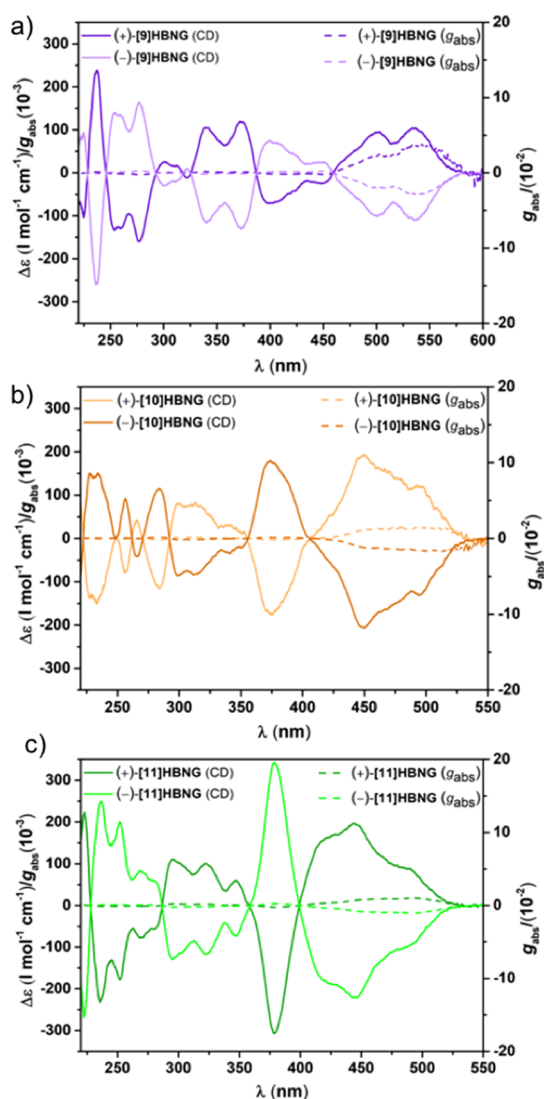


**Figure 7.** Circular dichroism spectra of (+)-[9]HBNG and (-)-[9]HBNG (a), (+)-[10]HBNG and (-)-[10]HBNG (b), and (+)-[11]HBNG and (-)-[11]HBNG (c). The CD spectrum of (+)-[10]HBNG (including  $g_{\text{abs}}$  factor) is corrected to optical purity (i.e., scaled by a factor of  $\sim 1.4$ ).

Helicenes have shown to display rather strong CPL activity with emission dissymmetry factor (i.e.,  $g_{\text{lum}}$ ) values as high as  $10^{-2}$ .<sup>42</sup> Recently, the possibility to incorporate heteroatoms (Si, S, B, N, and P) into helicene frameworks by using different synthetic strategies has attracted a special attention with the aim of creating structural diversity and tuning the photo-physical properties of such systems.<sup>43</sup> However, CPL-active all-carbon PAHs are still scarce, and the preparation of PAHs with strong CPL activity is still challenging.<sup>44</sup>

Interestingly, [10]HBNG and [11]HBNG exhibit intense CPL spectra, positive for the (*P*) enantiomers and negative for the (*M*) ones. Remarkable  $g_{\text{lum}}$  values (i.e.,  $g_{\text{lum}} = 2(I_{\text{L}} - I_{\text{R}})/(I_{\text{L}} + I_{\text{R}})$ ,  $I_{\text{L}}$  and  $I_{\text{R}}$  being the left- and right-handed luminescent emissions, respectively) were obtained. Indeed,  $g_{\text{lum}}$  values of  $+1.1 \times 10^{-2}/-1 \times 10^{-2}$  at 540 nm for (*P*)-[10]HBNG and (*M*)-[10]HBNG and of  $+8.4 \times 10^{-3}/-8.9 \times 10^{-3}$  at 535 nm for (*P*)-[11]HBNG and (*M*)-[11]HBNG were measured, respectively. Note that higher absolute values were found for the (*M*) enantiomers as compared to the (*P*) ones,

probably due to higher chemical and enantiomeric purities. Remarkably, much higher  $g_{\text{lum}}$  values were obtained for (*P*)-[9]HBNG and (*M*)-[9]HBNG, that is,  $+3.6 \times 10^{-2}/-3.6 \times 10^{-2}$  at 580 nm, respectively (Figure 8).

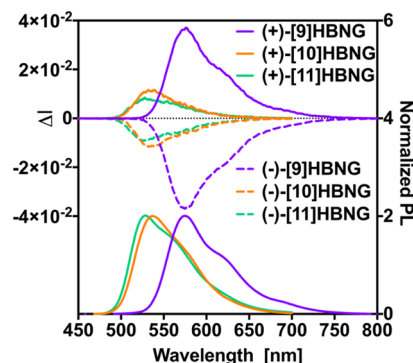


**Figure 8.** CPL/PL spectra of (*P*) and (*M*) enantiomers of [9]HBNG, [10]HBNG, and [11]HBNG in THF at room temperature and at concentrations around  $10^{-5}$  M.

The experimental values of  $g_{\text{lum}}$  agree very well with the theoretical values in Table 5 calculated from the quantum chemical quantities, such as the electric transition dipole moment (ETDM,  $\mu$ ) and the magnetic transition dipole moments (MTDM,  $m$ ) according to the equations

$$R = |\mu||m|\cos\theta$$

$$g_{\text{lum}} = (4|m|/|\mu|)\cos\theta$$

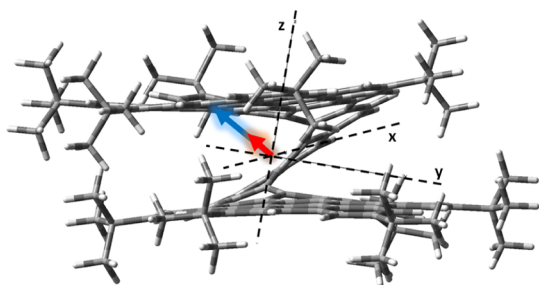
Table 5 summarizes the main values obtained with TD-DFT quantum chemical calculations for the three compounds. We adopt the accepted approximation of discussing the experimental  $g_{\text{lum}}$  compared with the computationally available  $g_{\text{abs}}$  when emission and absorption correspond to the same lowest energy electronic transition. The dissection of the  $g_{\text{abs}}$  values in terms of the microscopic quantum chemical quantities allows us to provide guidelines to account for the different chiroptical performance of the three compounds. First, TD-DFT calculations nicely predict the experimental variation of the  $g_{\text{lum}}$  in the three compounds as well as their order of magnitude. The largest value is found out in [9]HBNG with a value above  $10^{-2}$  which is very remarkable for organic pure hydrocarbon dyes. On the other hand, the values for [10]HBNG and [11]HBNG are smaller by a factor close to 4 in good agreement with experiments. We have found out that the moduli of the ETDM and MTDM transition vectors are the largest in [9]HBNG, whereas displaying the smallest/largest angle/cosine between them; thus, the three factors add to produce the largest  $g_{\text{abs}}$  for [9]HBNG (Figures 9 and S25, see the Supporting Information, show the direction and moduli of the ETDM and MTDM for the three systems). This fact points out to the design in [9]HBNG to be optimal for  $g_{\text{abs}}$ . The largest value for ETDM in [9]HBNG comes from a significant extension of the optical HOMO-to-LUMO one-electron excitation over the more planar HBC moiety, a situation that is more favorable in [9]HBNG because of the smallest helicene segment. On the other hand, the largest MTDM module, conversely, arises because there is a significant extension, among the three compounds, of the HOMO-LUMO excitation over the helicene curvature, thus promoting a pseudo-local rotation of the electron density

**Table 5. TD-DFT/B3LYP/6-31G\*\* Quantum Chemical Calculations of the Relevant Quantities Defining the  $g_{\text{abs}}$  for the Three Compounds**

	wavelength <sup>a</sup>	oscillator strength ( $f$ ) <sup>b</sup>	ETDM ( $\mu$ ) module <sup>c</sup>	MTDM ( $m$ ) module <sup>d</sup>	ETDM/MTDM angle ( $\theta$ ) <sup>e</sup>	rotational strength ( $R$ ) <sup>f</sup>	$10^2 \times$ dissymmetry factor ( $g_{\text{lum}}$ ) <sup>g</sup>
[9]HBNG	406.6	0.0771	1.0160	2.6270	3.4	$2.664 \times 10^{-39}$	1.03
[10]HBNG	404.4	0.0671	0.9453	1.4014	17.78	$1.261 \times 10^{-39}$	0.56
[11]HBNG	389.5	0.0548	0.8385	1.7485	63.51	$0.654 \times 10^{-39}$	0.37

<sup>a</sup>In nanometers. <sup>b</sup>In atomic units. <sup>c</sup>Electric transition dipole moments in  $10^{-18}$  esu-cm. <sup>d</sup>Magnetic transition dipole moments in  $10^{-21}$  erg/Gauss.

<sup>e</sup>In degrees. <sup>f</sup>In erg esu cm/Gauss. <sup>g</sup>Dimensionless values.

**Figure 9.** Directions and moduli of the ETDM (blue arrow) and MTDM (red arrows) in [9]HBNG.

during HOMO–LUMO excitation at the origin of the MTDM. This interpretation is supported by the electrochemical data: (i) the smallest oxidation potential of the three compounds in [9]HBNG indicates an important extension of the HOMO, among the three compounds, in the HBC units further helped by the inter-layer interaction. (ii) The smallest potential for the first reduction in [9]HBNG supports that the LUMO is greatly extended over the helicene but also with participation of the HBC unit. This synergistic combination of the frontier HOMO and LUMO orbitals between the helicene and the HBC produces the optimal situation for the increment of  $g_{\text{lum}}$ .

As proposed by Zinna and co-workers,<sup>45</sup> one may consider the brightness, defined as  $B_{\text{CPL}} = \epsilon \times \Phi \times g_{\text{lum}}/2$ . By this way, we take into account the overall process through absorption coefficient, emission quantum yield, and dissymmetry factor efficiencies. Average values of 81, 20, and 27 for [9]HBNG, [10]HBNG, and [11]HBNG, respectively, are obtained (Table 6). These values are significantly higher than the average  $B_{\text{CPL}}$  values of helicene derivatives ( $B_{\text{CPL}}$  14.10 for [9]helicenes and 1.35 for [11]helicenes)<sup>45</sup> and highlight the fact that a balanced  $\pi$ -extension of the chromophore between the planar HBC (promoting large ETDM) and the helicene

**Table 6. Experimental Data from the Circular Polarized Luminescence of the Enantioenriched HBNGs [9]HBNG, [10]HBNG, and [11]HBNG<sup>c</sup>**

	$\epsilon$ ( $\lambda_{\text{exc}}$ ) <sup>a,b</sup>	$\Phi_{\text{Fluo}}$ <sup>a</sup>	$10^2 \times g_{\text{lum}}$	$B_{\text{CPL}}$ <sup>b</sup>
(+)-[9]HBNG		22	+3.60	81
(-)-[9]HBNG	20,600 (440)		-3.60	81
(+)-[10]HBNG		10	+1.10 <sup>c</sup>	21 <sup>c</sup>
(-)-[10]HBNG	38,800 (420)		-1.00	19
(+)-[11]HBNG		11	+0.84	27
(-)-[11]HBNG	58,200 (420)		-0.89	28

<sup>a</sup> $\epsilon$  and  $\Phi_{\text{Fluo}}$  were obtained from the racemic mixture. <sup>b</sup> $\text{M}^{-1} \text{cm}^{-1}$ .

<sup>c</sup> $g_{\text{lum}}$  and  $B_{\text{CPL}}$  of (+)-[10]HBNG are corrected to optical purity (i.e., scaled by a factor of  $\sim 1.4$ ).

(promoting large MTDM) is an appealing alternative to obtain good emission and chiroptical properties.

## CONCLUSIONS

In summary, we have carried out the bottom-up synthesis of two new HBNGs, namely, [9]HBNG and [11]HBNG, following a similar methodology to that used for previously synthesized [10]HBNG. A full comparative spectroscopic (electronic, vibrational Raman, and chiroptical), electrochemical, and solid-state study of the three compounds is carried out. Interestingly, comparison of [9]HBNG, [10]HBNG, and [11]HBNG helical bilayers endowed with [9], [10], and [11]helicenes embedded in their structure, respectively, afford distinctive and unexpected properties, depending upon the overlapping degree between the two HBCs, determined from the X-ray data obtained for the three NGs.

The CV reveals, unexpectedly, the strongest electron donor character for the lesser  $\pi$ -extended system [9]HBNG, which is also supported by the spectroelectrochemical studies. The significant decrease of the oxidation potential observed for [9]HBNG and the red shift observed in the absorption bands of the radical cation of [9]HBNG have been accounted for by a charge delocalization between the two HBC layers, which eventually contributes to a lower oxidation potential. Actually, this inter-layer communication could also underpin the differences found in the fluorescence spectrum measured for [9]HBNG when compared to compounds [10]HBNG and [11]HBNG.

The differences observed for [9]HBNG, due to its strong overlapping between the two layers, is also found in the exceptional chiroptical properties that it exhibits, with values of  $g_{\text{lum}}$  as high as  $3.6 \times 10^{-2}$ .

Thus, the experimental findings show that this type of HBNG, formed by two  $\pi$ - $\pi$  stacked HBCs covalently connected through a (chiral) helicene, resembles vdW layered 2D materials, where the overlapping between the layers defines the properties of the materials. These findings pave the way to new NGs whose properties can be controlled by the length of the embedded helicene and the inter-layer interactions.

## ASSOCIATED CONTENT

### Supporting Information

The Supporting Information is available free of charge at <https://pubs.acs.org/doi/10.1021/jacs.3c01088>.

Synthetic procedures, additional figures/schemes of physical properties, and characterization data (PDF)

### Accession Codes

CCDC 2233478–2233479 contain the supplementary crystallographic data for this paper. These data can be obtained free of charge via [www.ccdc.cam.ac.uk/data\\_request/cif](http://www.ccdc.cam.ac.uk/data_request/cif), or by

emailing [data\\_request@ccdc.cam.ac.uk](mailto:data_request@ccdc.cam.ac.uk), or by contacting The Cambridge Crystallographic Data Centre, 12 Union Road, Cambridge CB2 1EZ, UK; fax: +44 1223 336033.

## AUTHOR INFORMATION

### Corresponding Author

**Nazario Martín** – Departamento de Química Orgánica I, Facultad de Ciencias Químicas, Universidad Complutense de Madrid, 28040 Madrid, Spain; IMDEA-Nanociencia, 28049 Madrid, Spain; [orcid.org/0000-0002-5355-1477](https://orcid.org/0000-0002-5355-1477); Email: [nazmar@ucm.es](mailto:nazmar@ucm.es)

### Authors

**Patricia Izquierdo-García** – Departamento de Química Orgánica I, Facultad de Ciencias Químicas, Universidad Complutense de Madrid, 28040 Madrid, Spain; [orcid.org/0000-0002-5004-1375](https://orcid.org/0000-0002-5004-1375)

**Jesús M. Fernández-García** – Departamento de Química Orgánica I, Facultad de Ciencias Químicas, Universidad Complutense de Madrid, 28040 Madrid, Spain; [orcid.org/0000-0002-7366-6845](https://orcid.org/0000-0002-7366-6845)

**Samara Medina Rivero** – Department of Physical Chemistry, Facultad de Ciencias, Universidad de Málaga, 29071 Málaga, Spain; Department of Physics & Astronomy, University of Sheffield, S3 7RH Sheffield, U.K.

**Michal Sámal** – Institute of Organic Chemistry and Biochemistry, Czech Academy of Sciences, 166 10 Prague 6, Czech Republic

**Jiří Rybáček** – Institute of Organic Chemistry and Biochemistry, Czech Academy of Sciences, 166 10 Prague 6, Czech Republic

**Lucie Bednářová** – Institute of Organic Chemistry and Biochemistry, Czech Academy of Sciences, 166 10 Prague 6, Czech Republic

**Sergio Ramírez-Barroso** – Departamento de Química Orgánica I, Facultad de Ciencias Químicas, Universidad Complutense de Madrid, 28040 Madrid, Spain; [orcid.org/0000-0001-8161-7296](https://orcid.org/0000-0001-8161-7296)

**Francisco J. Ramírez** – Department of Physical Chemistry, Facultad de Ciencias, Universidad de Málaga, 29071 Málaga, Spain; [orcid.org/0000-0002-8149-9143](https://orcid.org/0000-0002-8149-9143)

**Rafael Rodríguez** – Institut des Sciences Chimiques de Rennes (ISCR), UMR 6226 CNRS—Univ Rennes, 35000 Rennes, France

**Josefina Perles** – Laboratorio DRX Monocristal, SIdI, Universidad Autónoma de Madrid, 28049 Madrid, Spain; [orcid.org/0000-0003-0256-0186](https://orcid.org/0000-0003-0256-0186)

**David García-Fresnadillo** – Departamento de Química Orgánica I, Facultad de Ciencias Químicas, Universidad Complutense de Madrid, 28040 Madrid, Spain; [orcid.org/0000-0001-7348-7583](https://orcid.org/0000-0001-7348-7583)

**Jeanne Crassous** – Institut des Sciences Chimiques de Rennes (ISCR), UMR 6226 CNRS—Univ Rennes, 35000 Rennes, France; [orcid.org/0000-0002-4037-6067](https://orcid.org/0000-0002-4037-6067)

**Juan Casado** – Department of Physical Chemistry, Facultad de Ciencias, Universidad de Málaga, 29071 Málaga, Spain; [orcid.org/0000-0003-0373-1303](https://orcid.org/0000-0003-0373-1303)

**Irena G. Stará** – Institute of Organic Chemistry and Biochemistry, Czech Academy of Sciences, 166 10 Prague 6, Czech Republic; [orcid.org/0000-0002-5267-9604](https://orcid.org/0000-0002-5267-9604)

Complete contact information is available at: <https://pubs.acs.org/10.1021/jacs.3c01088>

## Notes

The authors declare no competing financial interest.

## ACKNOWLEDGMENTS

Financial support from the Spanish MICINN (Project PID2020-114653RB-I00) is acknowledged. N.M. and J.M.F.-G. thank the financial support by the ERC (SyG TOMATTO ERC-2020-951224). We also thank the support from the “(MAD2D-CM)-UCM” project funded by Comunidad de Madrid, by the Recovery, Transformation and Resilience Plan, and by NextGenerationEU from the European Union. S.M.R. thanks the UMA for her Margarita Salas postdoctoral fellowship under the “Plan de Recuperación, Transformación y Resiliencia” funded by European Union-Next Generation EU and the Spanish Ministry of Universities. S.M.R., F.J.R., and J.C. also thank the Research Central Services (SCAI) of the University of Málaga. J.C. acknowledges the Ministère de l'Éducation Nationale, de la Recherche et de la Technologie, and the Centre National de la Recherche Scientifique (CNRS). IGS acknowledges the financial support of the Czech Science Foundation (reg. no. 20-23566S) and the Institute of Organic Chemistry and Biochemistry, Czech Academy of Sciences (RVO: 61388963). RR thanks Xunta de Galicia for a postdoctoral fellowship.

## REFERENCES

- (1) Novoselov, K. S.; Geim, A. K.; Morozov, S. V.; Jiang, D.; Zhang, Y.; Dubonos, S. V.; Grigorieva, I. V.; Firsov, A. A. Electric field effect in atomically thin carbon films. *Science* **2004**, *306*, 666–669.
- (2) Hu, Y.; Wu, C.; Pan, Q.; Jin, Y.; Lyu, R.; Martínez, V.; Huang, S.; Wu, J.; Wayment, L. J.; Clark, N. A.; Raschke, M. B.; Zhao, Y.; Zhang, W. Synthesis of  $\gamma$ -graphyne using dynamic covalent chemistry. *Nat. Synth.* **2022**, *1*, 449–454.
- (3) Mannix, A. J.; Zhou, X. F.; Kiraly, B.; Wood, J. D.; Alducin, D.; Myers, B. D.; Liu, X.; Fisher, B. L.; Santiago, U.; Guest, J. R.; Yacaman, M. J.; Ponce, A.; Oganov, A. R.; Hersam, M. C.; Guisinger, N. P. Synthesis of borophenes: Anisotropic, two-dimensional boron polymorphs. *Science* **2015**, *350*, 1513–1516.
- (4) Dávila, M. E.; Xian, L.; Cahangirov, S.; Rubio, A.; Le Lay, G. Germanene: a novel two-dimensional germanium allotrope akin to graphene and silicene. *New J. Phys.* **2014**, *16*, 095002.
- (5) Vogt, P.; De Padova, P.; Quaresima, C.; Avila, J.; Frantzeskakis, E.; Asensio, M. C.; Resta, A.; Ealet, B.; Le Lay, G. Silicene: Compelling Experimental Evidence for Graphenelike Two-Dimensional Silicon. *Phys. Rev. Lett.* **2012**, *108*, 155501.
- (6) Zhu, F. F.; Chen, W. J.; Xu, Y.; Gao, C. L.; Guan, D. D.; Liu, C. H.; Qian, D.; Zhang, S. C.; Jia, J. F. Epitaxial growth of two-dimensional stanene. *Nat. Mater.* **2015**, *14*, 1020–1025.
- (7) Yuhara, J.; He, B.; Matsunami, N.; Nakatake, M.; Le Lay, G. Graphene's Latest Cousin: Plumbene Epitaxial Growth on a “Nano WaterCube”. *Adv. Mater.* **2019**, *31*, 1901017.
- (8) Liu, H.; Neal, A. T.; Zhu, Z.; Luo, Z.; Xu, X.; Tománek, D.; Ye, P. D. Phosphorene: An Unexplored 2D Semiconductor with a High Hole Mobility. *ACS Nano* **2014**, *8*, 4033–4041.
- (9) Martínez-Periñán, E.; Down, M. P.; Gibaja, C.; Lorenzo, E.; Zamora, F.; Banks, C. E. Antimonene: A Novel 2D Nanomaterial for Supercapacitor Applications. *Adv. Energy Mater.* **2018**, *8*, 1702606.
- (10) Reis, F.; Li, G.; Dudy, L.; Bauernfeind, M.; Glass, S.; Hanke, W.; Thomale, R.; Schäfer, J.; Claessen, R. Bismuthene on a SiC substrate: A candidate for a high-temperature quantum spin Hall material. *Science* **2017**, *357*, 287–290.
- (11) (a) Xiao, X.; Wang, H.; Urbankowski, P.; Gogotsi, Y. Topochemical synthesis of 2D materials. *Chem. Soc. Rev.* **2018**, *47*, 8744–8765. (b) Chowdhury, T.; Sadler, E. C.; Kempa, T. J. Progress and Prospects in Transition-Metal Dichalcogenide Research Beyond 2D. *Chem. Rev.* **2020**, *120*, 12563–12591. (c) VahidMohammadi, A.;

- Rosen, J.; Gogotsi, Y. The world of two-dimensional carbides and nitrides (MXenes). *Science* **2021**, 372, No. eabf1581. (d) Wu, G.; Liang, R.; Ge, M.; Sun, G.; Zhang, Y.; Xing, G. Surface Passivation Using 2D Perovskites toward Efficient and Stable Perovskite Solar Cells. *Adv. Mater.* **2022**, 34, 2105635.
- (12) Anichini, C.; Czepa, W.; Pakulski, D.; Aliprandi, A.; Ciesielski, A.; Samori, P. Chemical Sensing with 2D Materials. *Chem. Soc. Rev.* **2018**, 47, 4860–4908.
- (13) Das, S.; Pandey, D.; Thomas, J.; Roy, T. The Role of Graphene and Other 2D Materials in Solar Photovoltaics. *Adv. Mater.* **2019**, 31, 1802722.
- (14) Wang, Z.; Jingjing, Q.; Wang, X.; Zhang, Z.; Chen, Y.; Huang, X.; Huang, W. Two-dimensional light-emitting materials: preparation, properties and applications. *Chem. Soc. Rev.* **2018**, 47, 6128–6174.
- (15) Iannaccone, G.; Bonaccorso, F.; Colombo, L.; Fiori, G. Quantum engineering of transistors based on 2D materials heterostructures. *Nat. Nanotechnol.* **2018**, 13, 183–191.
- (16) Sherrell, P. C.; Fronzi, M.; Shepelin, N. A.; Corletto, A.; Winkler, D. A.; Ford, M.; Shapter, J. G.; Ellis, A. V. A bright future for engineering piezoelectric 2D crystals. *Chem. Soc. Rev.* **2022**, 51, 650–671.
- (17) Qiu, D.; Gong, C.; Wang, S.; Zhang, M.; Yang, C.; Wang, X.; Xiong, J. Recent Advances in 2D Superconductors. *Adv. Mater.* **2021**, 33, 2006124.
- (18) Gibertini, M.; Koperski, M.; Morpurgo, A. F.; Novoselov, K. S. Magnetic 2D materials and heterostructures. *Nat. Nanotechnol.* **2019**, 14, 408–419.
- (19) (a) Terrones, H.; López-Urías, F.; Terrones, M. Novel Hetero-Layered Materials with Tunable Direct Band Gaps by Sandwiching Different Metal Disulfides and Diselenides. *Sci. Rep.* **2013**, 3, 1549. (b) Robinson, J. A. Growing Vertical in the Flatland. *ACS Nano* **2016**, 10, 42–45. (c) Lam, D.; Lebedev, D.; Hersam, M. C. Morphotaxy of Layered van der Waals Materials. *ACS Nano* **2022**, 16, 7144–7167.
- (20) Andrei, E. Y.; Efetov, D. K.; Jarillo-Herrero, P.; MacDonald, A. H.; Mak, K. F.; Senthil, T.; Tutuc, E.; Yazdani, A.; Young, A. F. The marvels of moiré materials. *Nat. Rev. Mater.* **2021**, 6, 201–206.
- (21) Cao, Y.; Fatemi, V.; Demir, A.; Fang, S.; Tomarken, S. L.; Luo, J. Y.; Sanchez-Yamagishi, J. D.; Watanabe, K.; Taniguchi, T.; Kaxiras, E.; Ashoori, R. C.; Jarillo-Herrero, P. Correlated insulator behaviour at half-filling in magic-angle graphene superlattices. *Nature* **2018**, 556, 80–84.
- (22) Lilia, B.; Hennig, R.; Hirschfeld, P.; Profeta, G.; Sanna, A.; Zurek, E.; Pickett, W. E.; Amsler, M.; Dias, R.; Eremets, M. I.; Heil, C.; Hemley, R. J.; Liu, H.; Ma, Y.; Pierleoni, C.; Kolmogorov, A. N.; Rybin, N.; Novoselov, D.; Anisimov, V.; Oganov, A. R.; Pickard, C. J.; Bi, T.; Arita, R.; Errea, I.; Pellegrini, C.; Requist, R.; Gross, E. K. U.; Margine, E. R.; Xie, S. R.; Quan, Y.; Hire, A.; Fanfarillo, L.; Stewart, G. R.; Hamlin, J. J.; Stanev, V.; Gonnelli, R. S.; Piatti, E.; Romanin, D.; Daghero, D.; Valenti, R. The 2021 room-temperature superconductivity roadmap. *J. Phys.: Condens. Matter* **2022**, 34, 183002.
- (23) (a) Liu, J.; Feng, X. Synthetic Tailoring of Graphene Nanostructures with Zigzag-Edged Topologies: Progress and Perspectives. *Angew. Chem., Int. Ed.* **2020**, 59, 23386–23401. (b) González-Herrero, H.; Mendieta-Moreno, J. I.; Edalatmanesh, S.; Santos, J.; Martín, N.; Écija, D.; Torre, B.; Jelinek, P. Atomic Scale Control and Visualization of Topological Quantum Phase Transition in  $\pi$ -Conjugated Polymers Driven by Their Length. *Adv. Mat.* **2021**, 33, 2104495. (c) Li, S.-Y.; He, L. Recent progresses of quantum confinement in graphene quantum dots. *Front. Phys.* **2021**, 17, 33201.
- (24) (a) Wang, H.; Wang, H. S.; Ma, C.; Chen, L.; Jiang, C.; Chen, C.; Xie, X.; Li, A.-P.; Wang, X. Graphene nanoribbons for quantum electronics. *Nat. Rev. Phys.* **2021**, 3, 791–802. (b) Gu, Y.; Qiu, Z.; Müllen, K. Nanographenes and Graphene Nanoribbons as Multitalents of Present and Future Materials Science. *J. Am. Chem. Soc.* **2022**, 144, 11499–11524.
- (25) Liu, Z.; Fu, S.; Liu, X.; Narita, A.; Samori, P.; Bonn, M.; Wang, H. I. Small Size, Big Impact: Recent Progress in Bottom-Up Synthesized Nanographenes for Optoelectronic and Energy Applications. *Adv. Sci.* **2022**, 9, 2106055.
- (26) (a) Narita, A.; Wang, X. Y.; Feng, X.; Müllen, K. New advances in nanographene chemistry. *Chem. Soc. Rev.* **2015**, 44, 6616–6643. (b) Grzybowski, M.; Sadowski, B.; Butenschon, H.; Gryko, D. T. Synthetic Applications of Oxidative Aromatic Coupling-From Biphenols to Nanographenes. *Angew. Chem., Int. Ed.* **2020**, 59, 2998–3027. (c) Jassas, R. S.; Mughal, E. U.; Sadiq, A.; Alsantali, R. I.; Al-Rooqi, M. M.; Naeem, N.; Moussa, Z.; Ahmed, S. A. Scholl reaction as a powerful tool for the synthesis of nanographenes: a systematic review. *RSC Adv.* **2021**, 11, 32158–32202.
- (27) (a) Rickhaus, M.; Mayor, M.; Juriček, M. Chirality in curved polyaromatic systems. *Chem. Soc. Rev.* **2017**, 46, 1643–1660. (b) Pun, S. H.; Miao, Q. Toward Negatively Curved Carbons. *Acc. Chem. Res.* **2018**, 51, 1630–1642. (c) Fernández-García, J. M.; Evans, P. J.; Medina Rivero, S.; Fernández, I.; García-Fresnadillo, D.; Perles, J.; Casado, J.; Martín, N.  $\pi$ -Extended Corannulene-Based Nanographenes: Selective Formation of Negative Curvature. *J. Am. Chem. Soc.* **2018**, 140, 17188–17196. (d) Majewski, M. A.; Stępień, M. Bowls, Hoops, and Saddles: Synthetic Approaches to Curved Aromatic Molecules. *Angew. Chem., Int. Ed.* **2019**, 58, 86–116. (e) Urieta-Mora, J.; Krug, M.; Alex, W.; Perles, J.; Fernandez, I.; Molina-Ontoria, A.; Guldi, D. M.; Martín, N. Homo and Hetero Molecular 3D Nanographenes Employing a Cyclooctatetraene Scaffold. *J. Am. Chem. Soc.* **2020**, 142, 4162–4172. (f) Stuparu, M. C. Corannulene: A Curved Polyarene Building Block for the Construction of Functional Materials. *Acc. Chem. Res.* **2021**, 54, 2858–2870. (g) Chaolumen; Stepek, I. A.; Yamada, K. E.; Ito, H.; Itami, K. Construction of Heptagon-Containing Molecular Nanocarbons. *Angew. Chem., Int. Ed.* **2021**, 60, 23508–23532. (h) Zank, S.; Fernández-García, J. M.; Stasyuk, A. J.; Voityuk, A. A.; Krug, M.; Solà, M.; Guldi, D. M.; Martín, N. Initiating Electron Transfer in Doubly Curved Nanographene Upon Supramolecular Complexation of C<sub>60</sub>. *Angew. Chem., Int. Ed.* **2022**, 61, No. e202112834. (i) Zhou, Z.; Zhu, Y.; Fernández-García, J. M.; Wei, Z.; Fernández, I.; Petrukhina, M. A.; Martín, N. Stepwise reduction of a corannulene-based helical molecular nanographene with Na metal. *Chem. Commun.* **2022**, 58, 5574–5577. (j) González Miera, G.; Matsubara, S.; Kono, H.; Murakami, K.; Itami, K. Synthesis of octagon-containing molecular nanocarbons. *Chem. Sci.* **2022**, 13, 1848–1868.
- (28) (a) Rickhaus, M.; Mayor, M.; Juriček, M. Strain-induced helical chirality in polyaromatic systems. *Chem. Soc. Rev.* **2016**, 45, 1542–1556. (b) Cruz, C. M.; Márquez, I. R.; Mariz, I. F. A.; Blanco, V.; Sánchez-Sánchez, C.; Sobrado, J. M.; Martín-Gago, J. A.; Cuerva, J. M.; Maçoas, E.; Campaña, A. G. Enantiopure distorted ribbon-shaped nanographene combining two-photon absorption-based upconversion and circularly polarized luminescence. *Chem. Sci.* **2018**, 9, 3917–3924. (c) Ma, S.; Gu, J.; Lin, C.; Luo, Z.; Zhu, Y.; Wang, J. Supertwistacene: A Helical Graphene Nanoribbon. *J. Am. Chem. Soc.* **2020**, 142, 16887–16893. (d) Izquierdo-García, P.; Fernández-García, J. M.; Fernández, I.; Perles, J.; Martín, N. Helically Arranged Chiral Molecular Nanographenes. *J. Am. Chem. Soc.* **2021**, 143, 11864–11870. (e) Izquierdo-García, P.; Fernández-García, J. M.; Perles, J.; Fernández, I.; Martín, N. Electronic Control of the Scholl Reaction: Selective Synthesis of Spiro vs Helical Nanographenes. *Angew. Chem., Int. Ed.* **2023**, 62, No. e202215655.
- (29) (a) Zhu, Y.; Guo, X.; Li, Y.; Wang, J. Fusing of Seven HBCs toward a Green Nanographene Propeller. *J. Am. Chem. Soc.* **2019**, 141, 5511–5517. (b) Medel, M. A.; Cruz, C. M.; Miguel, D.; Blanco, V.; Morcillo, S. P.; Campaña, A. G. Chiral Distorted Hexa-perihexabenzocoronenes Bearing a Nonagon-Embedded Carbohelixene. *Angew. Chem., Int. Ed.* **2021**, 60, 22051–22056. (c) Reger, D.; Haines, P.; Amsharov, K. Y.; Schmidt, J. A.; Ullrich, T.; Bonisch, S.; Hampel, F.; Gorling, A.; Nelson, J.; Jelfs, K. E.; Guldi, D. M.; Jux, N. A Family of Superhelixenes: Easily Tunable, Chiral Nanographenes by Merging Helicity with Planar  $\pi$  Systems. *Angew. Chem., Int. Ed.* **2021**, 60, 18073–18081. (d) Zhou, Z.; Fernández-García, J. M.; Zhu, Y.; Evans, P. J.; Rodríguez, R.; Crassous, J.; Wei, Z.; Fernández, I.; Petrukhina, M. A.; Martín, N. Site-Specific Reduction-Induced Hydrogenation of a Helical Bilayer Nanographene with K and Rb Metals: Electron

Multiaddition and Selective Rb(+) Complexation. *Angew. Chem., Int. Ed.* **2022**, *61*, No. e202115747.

(30) (a) Fernández-García, J. M.; Evans, P. J.; Filippone, S.; Herranz, M. A.; Martín, N. Chiral Molecular Carbon Nanostructures. *Acc. Chem. Res.* **2019**, *52*, 1565–1574. (b) Fernández-García, J. M.; Izquierdo-García, P.; Buendia, M.; Filippone, S.; Martín, N. Synthetic chiral molecular nanographenes: the key figure of the racemization barrier. *Chem. Commun.* **2022**, *58*, 2634–2645.

(31) (a) Brandt, J. R.; Salerno, F.; Fuchter, M. J. The added value of small-molecule chirality in technological applications. *Nat. Rev. Chem.* **2017**, *1*, 0045. (b) Qiu, Z. J.; Ju, C. W.; Frederic, L.; Hu, Y. B.; Schollmeyer, D.; Pieters, G.; Müllen, K.; Narita, A. Amplification of Dissymmetry Factors in  $\pi$ -Extended [7]- and [9]Helicenes. *J. Am. Chem. Soc.* **2021**, *143*, 4661–4667. (c) Mori, T. Chiroptical Properties of Symmetric Double, Triple, and Multiple Helicenes. *Chem. Rev.* **2021**, *121*, 2373–2412. (d) Xiao, X.; Pedersen, S. K.; Aranda, D.; Yang, J.; Wiscons, R. A.; Pittelkow, M.; Steigerwald, M. L.; Santoro, F.; Schuster, N. J.; Nuckolls, C. Chirality Amplified: Long, Discrete Helicene Nanoribbons. *J. Am. Chem. Soc.* **2021**, *143*, 983–991.

(32) (a) Zhao, X. J.; Hou, H.; Fan, X. T.; Wang, Y.; Liu, Y. M.; Tang, C.; Liu, S. H.; Ding, P. P.; Cheng, J.; Lin, D. H.; Wang, C.; Yang, Y.; Tan, Y. Z. Molecular bilayer graphene. *Nat. Commun.* **2019**, *10*, 3057. (b) Milton, M.; Schuster, N. J.; Paley, D. W.; Hernández Sánchez, R.; Ng, F.; Steigerwald, M. L.; Nuckolls, C. Defying strain in the synthesis of an electroactive bilayer helicene. *Chem. Sci.* **2019**, *10*, 1029–1034. (c) Zhao, X. J.; Hou, H.; Ding, P. P.; Deng, Z. Y.; Ju, Y. Y.; Liu, S. H.; Liu, Y. M.; Tang, C.; Feng, L. B.; Tan, Y. Z. Molecular defect-containing bilayer graphene exhibiting brightened luminescence. *Sci. Adv.* **2020**, *6*, No. eaay8541.

(33) Buchta, M.; Rybáček, J.; Jančářík, A.; Kudale, A. A.; Buděšínský, M.; Vacek Chocholoušová, J.; Vacek, J.; Bednářová, L.; Císařová, I.; Bodwell, G. J.; Starý, I.; Stará, I. G. Chimerical Pyrene-based [7]Helicenes: A New Class of Twisted Polycondensed Aromatics. *Chem.—Eur. J.* **2015**, *21*, 8910–8917.

(34) Evans, P. J.; Ouyang, J.; Favereau, L.; Crassous, J.; Fernández, I.; Perles, J.; Martín, N. Synthesis of a Helical Bilayer Nanographene. *Angew. Chem., Int. Ed.* **2018**, *57*, 6774–6779.

(35) Stará, I. G.; Starý, I. *Synthesis of Helicenes by [2+2+2] Cycloisomerization of Alkynes and Related Systems Helicenes: Synthesis, Properties, and Applications*; Crassous, J., Stará, I. G., Starý, I., Eds.; Wiley-VCH: Weinheim, Germany, 2022; Chapter 2, pp 53–101.

(36) Nejedlý, J.; Šámal, M.; Rybáček, J.; Gay Sánchez, I.; Houska, V.; Warzecha, T.; Vacek, J.; Sieger, L.; Buděšínský, M.; Bednářová, L.; Fiedler, P.; Císařová, I.; Starý, I.; Stará, I. G. Synthesis of Racemic, Diastereopure, and Enantiopure Carba- or Oxa[5]-, [6]-, [7]-, and [19]helicene (Di)thiol Derivatives. *J. Org. Chem.* **2020**, *85*, 248–276.

(37) Stetsovych, O.; Mutombo, P.; Švec, M.; Šámal, M.; Nejedlý, J.; Císařová, I.; Vazquez, H.; Moro-Lagares, M.; Berger, J.; Vacek, J.; Stará, I. G.; Starý, I.; Jelínek, P. Large Converse Piezoelectric Effect Measured on a Single Molecule on a Metallic Surface. *J. Am. Chem. Soc.* **2018**, *140*, 940–946.

(38) Stará, I. G.; Starý, I. Helically Chiral Aromatics: The Synthesis of Helicenes by [2 + 2 + 2] Cycloisomerization of  $\pi$ -Electron Systems. *Acc. Chem. Res.* **2020**, *53*, 144–158.

(39) (a) Salari, A. A. Detection of NO<sub>2</sub> by hexa-peri-hexabenzocoronene nanographene: A DFT study. *C. R. Chim.* **2017**, *20*, 758–764. (b) Chang, L.; Cui, W.; Vahabi, V. A density functional theory study on the Hexa-peri-hexabenzocoronene nanographene oxide. *J. Phys. Chem. Solids* **2020**, *140*, 109373.

(40) Sillen, A.; Engelborghs, Y. The Correct Use of “Average” Fluorescence Parameters. *Photochem. Photobiol.* **1998**, *67*, 475–486.

(41) (a) Han, J.; Guo, S.; Lu, H.; Liu, S.; Zhao, Q.; Huang, W. Recent Progress on Circularly Polarized Luminescent Materials for Organic Optoelectronic Devices. *Adv. Opt. Mater.* **2018**, *6*, 1800538. (b) Zhao, W.-L.; Li, M.; Lu, H.-Y.; Chen, C.-F. Advances in helicene derivatives with circularly polarized luminescence. *Chem. Commun.* **2019**, *55*, 13793–13803. (c) Crassous, J. *Circularly Polarized Luminescence of Isolated Small Organic Molecules*; Springer, 2020; p 53.

(42) Examples of helicenes displaying  $g_{lum}$  as high as  $10^{-2}$ :

(a) Kaseyama, T.; Furumi, S.; Zhang, X.; Tanaka, K.; Takeuchi, M. Hierarchical Assembly of a Phthalhydrazide-Functionalized Helicene. *Angew. Chem., Int. Ed.* **2011**, *50*, 3684–3687. (b) Shen, C.; Anger, E.; Srebro, M.; Vanthuyne, N.; Deol, K. K.; Jefferson, T. D.; Muller, G.; Williams, J. A. G.; Toupet, L.; Roussel, C.; Autschbach, J.; Réau, R.; Crassous, J. Straightforward access to mono- and bis-cycloplatinated helicenes displaying circularly polarized phosphorescence by using crystallization resolution methods. *Chem. Sci.* **2014**, *5*, 1915–1927. (c) Nakamura, K.; Furumi, S.; Takeuchi, M.; Shibuya, T.; Tanaka, K. Enantioselective Synthesis and Enhanced Circularly Polarized Luminescence of S-Shaped Double Azahelicenes. *J. Am. Chem. Soc.* **2014**, *136*, 5555–5558. (d) Murayama, K.; Oike, Y.; Furumi, S.; Takeuchi, M.; Noguchi, K.; Tanaka, K. Enantioselective Synthesis, Crystal Structure, and Photophysical Properties of a 1,1'-Bitriphenylene-Based Sila[7]helicene. *Eur. J. Org. Chem.* **2015**, *2015*, 1409–1414. (e) Schaack, C.; Arrico, L.; Sidler, E.; Górecki, M.; Di Bari, L.; Diederich, F. Helicene Monomers and Dimers: Chiral Chromophores Featuring Strong Circularly Polarized Luminescence. *Chem.—Eur. J.* **2019**, *25*, 8003–8007. (f) Dhbaibi, K.; Favereau, L.; Srebro-Hooper, M.; Quinton, C.; Vanthuyne, N.; Arrico, L.; Roisnel, T.; Jamoussi, B.; Poriel, C.; Cabanetos, C.; Autschbach, J.; Crassous, J. Modulation of circularly polarized luminescence through excited-state symmetry breaking and interbranched exciton coupling in helical push–pull organic systems. *Chem. Sci.* **2020**, *11*, 567–576. (g) Otani, T.; Sasayama, T.; Iwashimizu, C.; Kanyiva, K. S.; Kawai, H.; Shibata, T. Short-step synthesis and chiroptical properties of polyaza[5]–[9]helicenes with blue to green-colour emission. *Chem. Commun.* **2020**, *56*, 4484–4487. (h) Dhbaibi, K.; Abella, L.; Meunier-Della-Gatta, S.; Roisnel, T.; Vanthuyne, N.; Jamoussi, B.; Pieters, G.; Racine, B.; Quesnel, E.; Autschbach, J.; Crassous, J.; Favereau, L. Achieving high circularly polarized luminescence with push–pull helicenic systems: from rationalized design to top-emission CP-OLED applications. *Chem. Sci.* **2021**, *12*, 5522–5533. (i) Zhao, F.; Zhao, J.; Wang, Y.; Liu, H.-T.; Shang, Q.; Wang, N.; Yin, X.; Zheng, X.; Chen, P. [5]Helicene-based chiral triarylboranes with large luminescence dissymmetry factors over a  $10^{-2}$  level: synthesis and design strategy via isomeric tuning of steric substitutions. *Dalton Trans.* **2022**, *51*, 6226–6234. (j) Rodríguez, R.; Naranjo, C.; Kumar, A.; Matozzo, P.; Das, T. K.; Zhu, Q.; Vanthuyne, N.; Gómez, R.; Naaman, R.; Sánchez, L.; Crassous, J. Mutual Monomer Orientation To Bias the Supramolecular Polymerization of [6]Helicenes and the Resulting Circularly Polarized Light and Spin Filtering Properties. *J. Am. Chem. Soc.* **2022**, *144*, 7709–7719.

(43) Dhbaibi, K.; Favereau, L.; Crassous, J. Enantioenriched Helicenes and Helicenoids Containing Main-Group Elements (B, Si, N, P). *Chem. Rev.* **2019**, *119*, 8846–8953.

(44) (a) Sawada, Y.; Furumi, S.; Takai, A.; Takeuchi, M.; Noguchi, K.; Tanaka, K. Rhodium-Catalyzed Enantioselective Synthesis, Crystal Structures, and Photophysical Properties of Helically Chiral 1,1'-Bitriphenylenes. *J. Am. Chem. Soc.* **2012**, *134*, 4080–4083. (b) Shen, C.; Gan, F.; Zhang, G.; Ding, Y.; Wang, J.; Wang, R.; Crassous, J.; Qiu, H. Helicene-derived aggregation-induced emission conjugates with highly tunable circularly polarized luminescence. *Mater. Chem. Front.* **2020**, *4*, 837–844. (c) Xu, Q.; Wang, C.; He, J.; Li, X.; Wang, Y.; Chen, X.; Sun, D.; Jiang, H. Corannulene-based nanographene containing helical motifs. *Org. Chem. Front.* **2021**, *8*, 2970–2976. (d) Shen, C.; Zhang, G.; Ding, Y.; Yang, N.; Gan, F.; Crassous, J.; Qiu, H. Oxidative cyclo-rearrangement of helicenes into chiral nanographenes. *Nat. Commun.* **2021**, *12*, 2786.

(45) Arrico, L.; Di Bari, L.; Zinna, F. Quantifying the Overall Efficiency of Circularly Polarized Emitters. *Chem.—Eur. J.* **2021**, *27*, 2920–2934.